nature electronics

SUPPLEMENTARY INFORMATION

https://doi.org/10.1038/s41928-019-0345-8

In the format provided by the authors and unedited.

# Ultrafast and energy-efficient spin–orbit torque switching in compensated ferrimagnets

**Kaiming Cai, Zhifeng Zhu, Jong Min Lee, Rahul Mishra, Lizhu Ren, Shawn D. Pollard, Pan He, Gengchiau Liang, Kie Leong Teo and Hyunsoo Yang***

Department of Electrical and Computer Engineering, National University of Singapore, Singapore, Singapore. *e-mail: eleyang@nus.edu.sg

**Supplementary Note 1: Identification of the magnetization and angular momentum compensation compositions**

For this study, a series of Pt (8 nm)/$Co_{100-x}Gd_x$ (5 nm)/$TaO_x$ (1 nm)/$SiO_2$ (4 nm) films, which exhibit bulk perpendicular magnetic anisotropy, were deposited by magnetron sputtering. The hysteresis loops were measured by polar magneto-optic Kerr effect (MOKE) and vibrating sample magnetometer (VSM). The divergence of $H_c$ indicates the magnetization compensation ($x_{MC}$)[1,2]. Moreover, the net magnetization $M_s$ also shows a minimum value around the magnetization compensation as shown in Supplementary Fig. 1a. Since the Kerr signal is mainly dominated by the Co sublattices[1], the absolute value of the change of Kerr signal, $|\Delta V_{Kerr}|$, between the "up" and "down" states gradually decreases with increasing the Gd concentration as shown in Supplementary Fig. 1a, which confirms the gradual change in the Co composition.

To accurately characterize the magnetic properties of $Co_{100-x}Gd_x$ in the vicinity of the $x_{MC}$, we further measure the temperature dependence of the magnetization $M(T)$ by superconducting quantum interference device (SQUID). The $M(T)$ curve of $Co_{74.5}Gd_{25.5}$ shows a distinct transition from Gd-rich to Co-rich with the magnetization compensation temperature $T_{MC}$ ~ 330 K. At the room temperature ($T_{RM}$ ~ 300 K), the $M_s$ of $Co_{74.5}Gd_{25.5}$ is ~7.1 emu $cm^{-3}$, which is slightly Gd-rich and very close to the magnetization compensation state. In addition, the $Co_{75}Gd_{25}$ film shows a Co-rich at room temperature. Thus, the compensation composition $x_{MC}$ should be between 25 and 25.5.

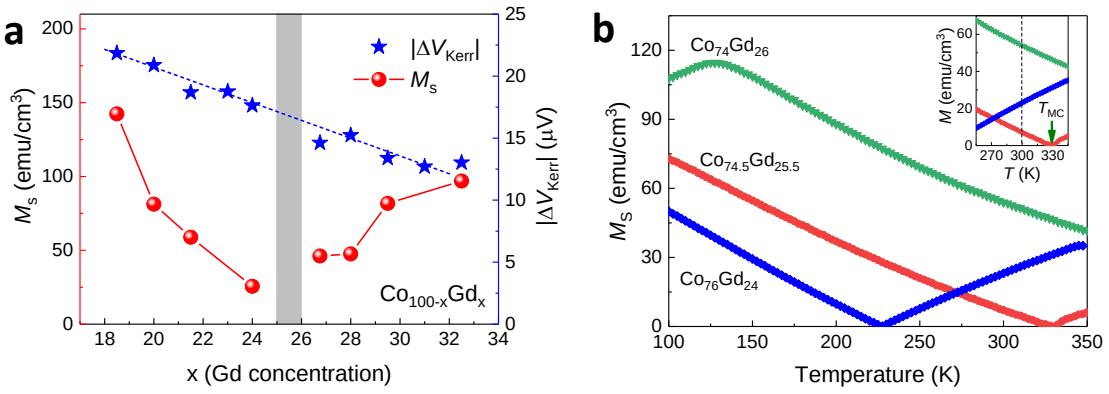


**Supplementary Figure 1 | Identification of magnetization compensation $x_{MC}$ and angular momentum compensation $x_{AMC}$. a**, Saturation magnetization of deposited films as a function of Gd concentration. The shaded region indicates the magnetization compensation. $|\Delta V_{Kerr}|$ indicate the absolute values of Kerr signal change. **b**, Temperature dependence of magnetization at $H$ = 2000 Oe in $Co_{76}Gd_{24}$ (blue), $Co_{74.5}Gd_{25.5}$ (red) and $Co_{74}Gd_{26}$ (green) at field cooling condition. Inset shows an enlargement of the magnetization compensation point ($T_{MC}$ ~ 330 K for $Co_{74.5}Gd_{25.5}$).

Although $x_{MC}$ and $T_{MC}$ can be determined by MOKE and VSM measurements, the $T_{AMC}$ is not easy to be determined. For CoGd ferrimagnets, the net magnetization $M_s$ and angular momentum $A_s$ are written as[3]: $M_s = M_{Co} - M_{Gd}$ and $A_s = A_{Co} - A_{Gd} = M_{Co}/\gamma_{Co} - M_{Gd}/\gamma_{Gd}$, where $M_{Co(Gd)}$ and $A_{Co(Gd)}$ are the magnetic moment and angular momentum of the Co(Gd) sublattices, respectively. The gyromagnetic ratio of Co ($\gamma_{Co}$) is slight larger than that of Gd ($\gamma_{Gd}$). Thus, the $T_{AMC}$ is expected to be higher than $T_{MC}$ ($T_{AMC} > T_{MC}$) in CoGd.

To identify the angular momentum compensation point ($x_{AMC}$) at the room temperature, we utilized a theoretical model based on the modified Landau-Lifshitz-Bloch (LLB) equation[4]:

$$\frac{d\mathbf{m}_v}{dt} = \gamma_v \left(\mathbf{m}_v \times \mathbf{H}_v^{MFA}\right) - \Gamma_{v,\parallel}\left(1 - \frac{\mathbf{m}_v \cdot \mathbf{m}_{0,v}}{\mathbf{m}_v^2}\right)\mathbf{m}_v - \Gamma_{v,\perp}\left(1 - \frac{\mathbf{m}_v \times \left(\mathbf{m}_v \times \mathbf{m}_{0,v}\right)}{\mathbf{m}_v^2}\right) \quad \text{(S1)}$$

, where $\mathbf{m}_v$ is the sublattice magnetization ($v$ denotes either TM or RE element), $\mathbf{m}_{0,v}$ is the equilibrium magnetization, $\gamma_v$ is the gyromagnetic constant, $\mathbf{H}_v^{MFA}$ is the mean field with considering the exchange coupling, and $\Gamma_{v,\parallel}$ and $\Gamma_{v,\perp}$ are the longitudinal and transverse damping coefficients, respectively. On the right side of the equation (S1), the first term describes the precession of magnetization, the second and the last terms introduce the longitudinal and transverse relaxation. Thus, the LLB model enables the systematic descriptions of the magnetization and angular momentum in ferrimagnets when the composition or temperature changes.

Based on the experimental results, the magnetization compensation point of our CoGd films is expected at $x_{MC}$ ~25.2 at room temperature. The LLB model was calibrated by matching the numerically obtained value with the experimental one $x_{MC}$ ~ 25.2. The key parameter of the exchange interaction $J_{RE\text{-}TM}$ between RE and TM was calibrated. Combined with the previously reported Landé $g$ factors of Co (~2.2) and Gd (~2) atoms[3-5], the net magnetization ($M_s$) and angular momentum compensation ($A_s$) as a function of concentration of Gd and temperature can be estimated using the LLB model. As shown in Supplementary Fig. 2a, $x_{AMC}$ ~23.3 is extracted, which is confirmed by $A_s(T) \approx 0$ at room temperature from the temperature dependence results of $Co_{76.7}Gd_{23.3}$ in Supplementary Fig. 2b.

To further confirm our calculated results, we used a theoretical prediction based on temperature dependence of sublattice magnetization using a power-law relation[6], which provides a linear relation between $T_{AMC}$ and $T_{MC}$ as $T_{AMC} = T_{MC} + \eta T_c$ in compensated ferrimagnets, here $\eta$ is the constant and $T_c$ is the Curie temperature. From the magnetization results of $Co_{76}Gd_{24}$ in Supplementary Fig. 1b measured by SQUID, $\eta$ and $T_c$ can be extracted[6] as ~0.30 and 519.8 K, respectively. Therefore, the $T_{AMC}$ of $Co_{76}Gd_{24}$ is estimated as ~382.6 K.

In addition, the $Co_{77.2}Gd_{22.8}$ is expected to be angular momentum compensated at room temperature, which is in good accordance with the results estimated by the LLB model. For our samples, the films of $Co_{76}Gd_{24}$ and $Co_{77}Gd_{23}$ are expected to have their $T_{AMC}$ around room temperature.

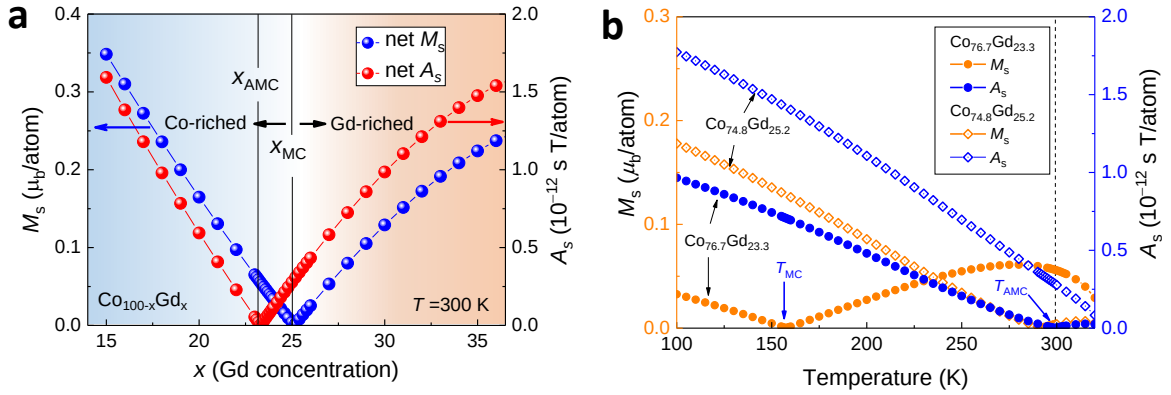


**Supplementary Figure 2 | Calculations of net magnetization $M_s$ and net angular momentum $A_s$ as a function of Gd concentration and temperature. a,** Gd concentration ($x$) dependence of the $M_s$ and $A_s$ at room temperature $T$ = 300 K. The calculated results show $Co_{74.8}Gd_{25.2}$ ($x \approx 25.2$) is the magnetization compensated composition and $Co_{76.7}Gd_{23.3}$ ($x \approx 23.3$) is the angular momentum compensated composition. **b,** Temperature dependence of the $M_s$ and $A_s$ for $Co_{76.7}Gd_{23.3}$ and $Co_{74.8}Gd_{25.2}$. The calculated $T_{AMC}$ of $Co_{76.7}Gd_{23.3}$ is close to the room temperature, at which it shows a Co-rich magnetization.

## Supplementary Note 2: Switching diagram with different pulse durations by all electrical measurements

We also investigate the SOT induced switching dynamics by measuring the switching probability with all electrical measurements. The switching probability is obtained by measuring the resistance of anomalous Hall effect ($R_{AHE}$) after injection of a current pulse with a current density $J$ and pulse duration $\tau_p$. For the measurements, the CoGd ferrimagnet films were patterned into a pillar with a diameter of 1000 nm on top of the Pt Hall cross. Sub-nanosecond current pulses were applied in the Pt channel and an external in-plane magnetic field $H_{ext}$ was applied to assist the deterministic SOT switching. The magnetization was initialized to a specific state by using a large d.c. current before applying the current pulses. The cumulative switching probability[7] is defined as

$$P_{SW}\left(J,\tau_p\right)=\left[R_{AHE}^{write}\left(J,\tau_p\right)-R_{AHE}^{reset}\right]\Big/\Delta R_{AHE} \quad \text{(S2)}$$

Here $R_{\mathrm{AHE}}^{\mathrm{write}}\left(J,\tau_{\mathrm{p}}\right)$ and $R_{\mathrm{AHE}}^{\mathrm{reset}}$ are the measured $R_{\mathrm{AHE}}$ after the pulse injection and after the initialization, respectively. $\Delta R_{\mathrm{AHE}}$ indicates the difference of $R_{\mathrm{AHE}}$ between "up" and "down" magnetization states. Each data point was acquired by averaging over 20 trials. The $J$ value of the injected pulse is determined by measuring the transmitted signal through the device.

Supplementary Fig. 3 shows the SOT switching results of the patterned Pt/$Co_{80.5}Gd_{19.5}$ device under nanosecond current pulses at $H_{\mathrm{ext}}$ = –630 Oe. The representative measurement of $P_{\mathrm{sw}}$ as a function of $\tau_{\mathrm{p}}$ for different values of $J$ is shown in Supplementary Fig. 3a. A "down" to "up" switching is observed upon injecting a positive current pulse with a negative $H_{\mathrm{ext}}$ is applied. The observed $P_{\mathrm{sw}}$ shows an increase with respect to $\tau_{\mathrm{p}}$. From the repeated $P_{\mathrm{sw}}$ measurements with varying $J$ and $\tau_{\mathrm{p}}$, the switching diagram is constructed as shown in Supplementary Fig. 3b, where the values of $J$ and $\tau_{\mathrm{p}}$ to achieve $P_{\mathrm{sw}}$ = 50% is defined as the critical switching current density ($J_{\mathrm{c}}$) and critical pulse duration ($\tau_{\mathrm{c}}$). The switching can be achieved with $\tau_{\mathrm{c}} \sim 0.45$ ns for $J_{\mathrm{c}} = 1.57 \times 10^{12}$ A m$^{-2}$.

The switching diagram indicates that the $J_{\mathrm{c}}$ decreases with a longer $\tau_{\mathrm{p}}$, which is expected from SOT-driven magnetization switching dynamics[7,8]. The switching diagram shows two distinct regimes in Supplementary Fig. 3b similar to the SOT switching in ferromagnets[7,9,10] such as spin-torque dominated regime at $\tau_{\mathrm{c}} < 2$ ns and the thermally activated regime at $\tau_{\mathrm{c}} > 2$ ns. The two regimes can be also observed between $J_{\mathrm{c}}$ and $1/\tau_{\mathrm{c}}$ in Supplementary Fig. 3c.

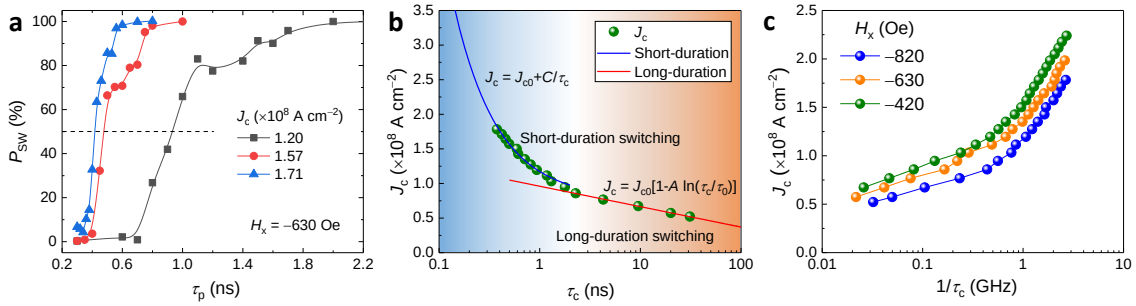


**Supplementary Figure 3 | SOT switching in a ferrimagnet by current pulses. a**, The measured switching probability of patterned Pt/$Co_{80.5}Gd_{19.5}$ device as a function of current pulse duration with varying the current density under an external magnetic field $H_x$ = –630 Oe. **b**, The measured critical switching current density and pulse width with $H_x$ = –630 Oe. Two distinct switching regimes: spin-torque dominated regime with $\tau_{\mathrm{c}} < 2$ ns and thermal activation with $\tau_{\mathrm{c}} > 2$ ns. **c,** The critical switching current density as a function of $1/\tau_{\mathrm{c}}$ with different magnetic fields.

## Supplementary Note 3: Comparisons of SOT switching between ferromagnets and ferrimagnets

The SOT switching process depends on the current density, external magnetic field, magnetic properties, and size of the device. Previous ferromagnet based SOT experiments showed that the gain in operation speed always comes at the expense of a rise in the current density[7,8]. It is generally difficult to keep a fast operation and low energy consumption at the same time. We compare the performance parameters of ferromagnet and ferrimagnet SOT devices. Given that the speed of switching (or domain wall motion) is proportional to the current density and the switching time is proportional to the lateral size of the device, we normalized the device size and scaled each parameter[11]. In addition, the normalized write energy $E_{sw} = I^2 R \tau_p$ is also evaluated for the different SOT systems, where $I$ is switching current, $R$ is the resistance of the channel, and $\tau_p$ is the pulse length. The results are summarized in Supplementary Table 1.

**Supplementary Table 1 | SOT switching time and pulse duration in ferromagnets and ferrimagnets.**

| Device Structure | Pulse duration | Current density (A m$^{-2}$) | Magnetic field (mT) | Switching time (ns) | Size (nm) | Normalized switching time (100 nm) | Write energy per unit area (mJ cm$^{-2}$) | Reference |
|---|---|---|---|---|---|---|---|---|
| Pt (3nm)/Co (0.6 nm)/$AlO_x$ | ~240 ps | $4.4\times10^{12}$ | 150 | ~1-1.4 | 90-100 | ~1 ns | 13.3 | [7] |
| Pt (5 nm)/Co (1 nm)/$AlO_x$ | 2 ns | $3.36\times10^{12}$ | 124 | 2 | 500 | 400 ps | 41.0 | [12] |
| Ta (3 nm)/Pt (8.5 nm)/Co (0.5 nm)/$Al_2O_3$ | 1 ns | $3.1\times10^{12}$ | 150 | 1.5 | 2000 | 75 ps | 6.30 | [13] |
| Pt (8 nm)/$Co_{76}Gd_{24}$ (5 nm) | **400 ps** | **$4.2\times10^{11}$** | **144.4** | **0.7** | **2800** | **25 ps** | **0.174** | This work |
| Ta (3 nm)/CoFeB (1.2 nm)/MgO | ~1.4 ns | $5.2\times10^{12}$ | 168 | 1.8 | 2000 | 90 ps | 15.0 | [14] |
| Ta (6 nm)/CoFeB (0.9 nm)/MgO | ~1 ns | $7.94\times10^{11}$ | 119.1 | ~2.2 | 1000 | ~220 ps | 4.10 | [10] |
| Ta (10 nm)/CoFeB (1 nm) | ~400 ps | $3.3\times10^{12}$ | 100 | ~0.9 | 150 | ~600 ps | 1867 | [8] |

Supplementary Fig. 4 shows the normalized write energy versus the pulse duration for Pt/Co[7], Ta/CoFeB[8], and Pt/CoGd systems. For comparison, all the results are from electrical measurements with similar conditions, and the lateral dimensions of devices are normalized to 100 nm. The energy consumption in our Pt/$Co_{80.5}Gd_{19.5}$ ferrimagnet device is estimated to be ~0.11-0.26 pJ, which is about one to two orders of magnitude smaller than that of ferromagnets.

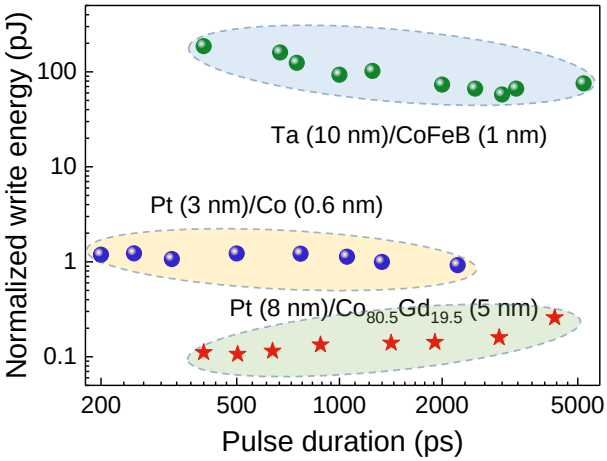


**Supplementary Figure 4 | Comparisons of energy consumption between ferromagnets and ferrimagnets.** The normalized write energy consumption versus the pulse duration in Pt (3 nm)/Co (0.6 nm)[7], Ta (10 nm)/CoFeB (1 nm)[8], and Pt (8 nm)/$Co_{80.5}Gd_{19.5}$ (5 nm), respectively.

**Supplementary Note 4: Domain nucleation and propagation in SOT switching process**

In order to evaluate the characteristics of the SOT switching process, we perform the time-resolved MOKE measurements by focusing the laser spot at different positions on the wire. The switching process was checked by applying pulse with a current density of $2.91\times10^{11}$ A $m^{-2}$ and longer duration (5 ns) to ensure a full switching. Time-resolved MOKE signals were acquired while moving the laser spot as shown in Supplementary Fig. 5a. As shown in Supplementary Fig. 5b, the switching process can be explained as follows. When the domain wall reaches the detection region, the Kerr signal starts to increase, corresponding to an arrival time $t_a$. The Kerr signal continues to increase as the domain wall goes through the laser spot region. Finally, the Kerr signal becomes constant after the domain wall moves out of the detection region. We observe that $t_a$ monotonically decreases as a function of the device position (Supplementary Fig. 5c). This suggests that a single domain nucleates at the right side and propagates to the left side of the wire during the magnetization switching.

During each reversal of magnetization switching, the domain wall traverses the probe region of the laser spot in a switching time $t_{sw}$. The domain wall velocity $v_{DW}$ can be evaluated as $v_{DW} \sim D/t_{sw,}$ where $D$ is the diameter of the laser spot[15]. Moreover, the linear fitting of the arrival time $t_a$ in Supplementary Fig. 5c indicates a stable domain propagation, corresponding to an average domain wall velocity of ~1351 m $s^{-1}$ with the current density $J = 2.91\times10^{11}$ A $m^{-2}$ and pulse duration $\tau_p$ = 5 ns, which is in line with the result of velocity using $v_{DW} \sim D/t_{sw}$ = 2.8 μm/2.2 ns = 1272 m $s^{-1}$.

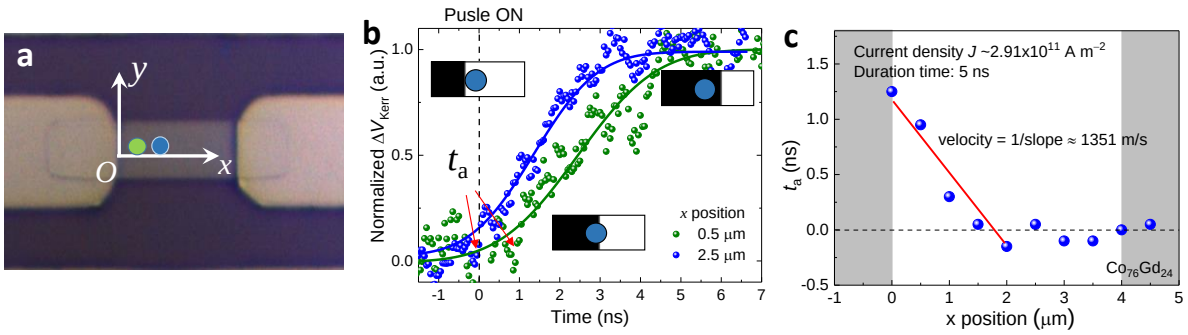


**Supplementary Figure 5 | Domain nucleation and propagation in the $Co_{76}Gd_{24}$ strip. a,** Optical image of the device. **b,** Temporal evolution of time-resolved MOKE signals with a laser spot focusing at different positions. **c,** Arrival time $t_a$ as a function of the central position $x$ of the laser spot.

We utilize an analytical model to interpret the SOT switching process and to extract the domain wall velocity[9,15] from the time resolved signal of Supplementary Fig. 5b. The change of the MOKE signal $S(t)$ can be expressed with an error function

$$S(t) \approx A erfc\left[\left(x(t)/R_0\right)\right] = A erfc\left[2\sqrt{2}v_{DW}\left(t_a - t\right)/D\right] \quad \text{(S3)}$$

, where the constant coefficient $A$ is related to the power, distribution, and absorption of the laser, as well as the properties of the magnetic films, such as the thickness and Kerr rotation. As shown in Supplementary Fig. 6b, the time-resolved result can be fitted with equation (S3). The domain velocity is extracted as ~1361 m $s^{-1}$ in $Co_{76}Gd_{24}$, with a current density ~ $2.91\times10^{11}$ A $m^{-2}$ and duration 5 ns, which is consistent with the results in Supplementary Fig. 5c.

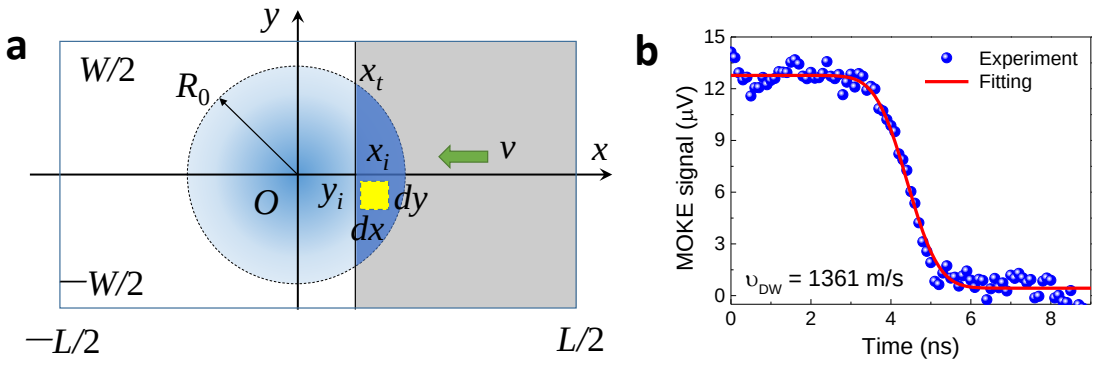


**Supplementary Figure 6 | Model of domain propagation and domain wall velocity. a**, Schematic illustration of the MOKE signal. The dashed circle is the detection region of the laser spot. The grey shaded region is the nucleated domain, which is propagating to the left side with a velocity of $v_{DW}$. **b**, Measured temporal evolution of MOKE signal in $Co_{76}Gd_{24}$ with the current density ~$2.91\times10^{11}$ A $m^{-2}$ and duration 5 ns. The red line presents a fit with $v_{DW}$ = ~1361 m $s^{-1}$.

**Supplementary Note 5: Device-size dependence of SOT switching in CoGd ferrimagnets**

To characterize and verify the dimensional scaling on the switching time and energy of the ultrafast switching, we fabricated Hall-cross devices with different diameters of magnetic pillars from the sputter-deposited film stacks of Pt (8 nm)/$Co_{79}Gd_{21}$ (5 nm) (as shown in Supplementary Fig. 7a). A series of devices were fabricated with various nominal diameters ($D$, ranging from 100 to 1500 nm) of nano-magnetic pillars on top of Hall cross channel. The width ($W$) and length ($L$) of the channel were scaled down with the ratios as $W/D$ = 1.5~1.9 and $L/D$ = 4~8, respectively. We repeated the switching probability measurements (Supplementary Note 2) on these devices by varying the pulse durations ($\tau$) under the similar pulse current density $J_p \sim 7.84\times10^{11}$ A m$^{-2}$ and the external magnetic field $H_x$ = –820 Oe. The critical pulse duration ($\tau_c$) for switching with $P_{SW}$ = 50% is extracted.

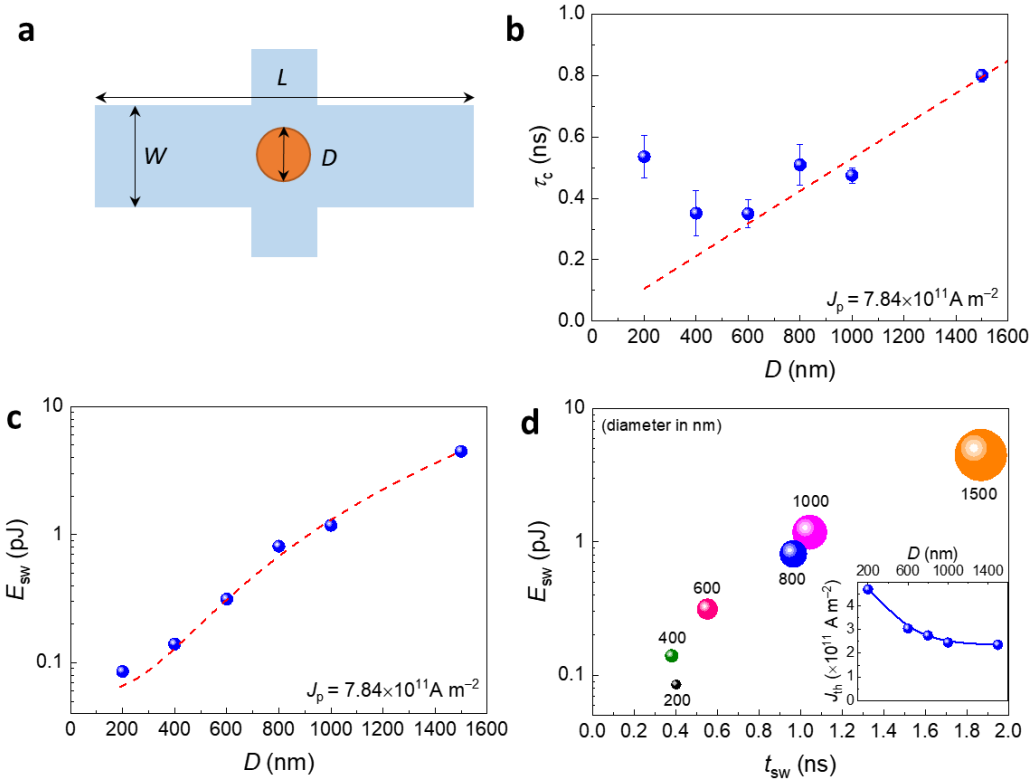


**Supplementary Figure 7 | Scaling of the switching time and energy consumption on ultrafast SOT switching in ferrimagnet CoGd**. **a**, Schematic of Hall-bar devices with the nominal diameter, channel width, and length. **b**, The extracted current pulse durations with switching probability $P_{SW}$ = 50% for different nano-pillar diameters. A pulse current density $J_p$ = $7.84\times10^{11}$ A m$^{-2}$ and an external magnetic field $H_x$ = –820 Oe was used during the measurements. The red line shows a linear fit. The error bars are the standard deviations from repeated measurements. **c**, The estimated energy consumption for magnetization switching. **d**, The characteristic switching time ($t_{sw}$) and energy consumption. The inset shows the critical dc switching current density $J_{th}$ of different sizes of the diameter, which was indicated next to dots.

Supplementary Fig. 7b shows measured data from devices. For the devices with $D > 400$ nm, the pulse width of the critical switching current $\tau_c$ decreases with shrinking the size of the devices. A linear scaling to $D$ (dash line in Supplementary Fig. 7b) is in accordance with the domain wall propagation for SOT switching[10,12]. The energy consumption ($E_{sw}$) during switching is estimated using $E_{sw} = I_p^2 R\tau_c$ (as shown in Supplementary Fig. 7c). Here, $I_p$ is the current flowing in the bottom Pt layer under the magnetic dot. The energy consumption is also comparable with the normalized results in Supplementary Note 3 and Fig. 2c in the main text.

The characteristic switching time ($t_{sw}$) is estimated using $J_p = J_{th}(1 + t_{sw}/\tau_c)$ (ref.[16]). Here, $J_{th}$ is the critical dc switching current. It should be noted that for the device with $D = 200$ nm the $\tau_c$ increases due to the increase in the effective anisotropy field as a result of reduced demagnetization for a smaller sized device[17]. As the dot diameter $D$ decreases from 1500 to 200 nm, the critical switching current density ($J_{th}$), measured by sweeping the dc current, increases by a factor of ~2 (inset of Supplementary Fig. 7d). The scaling of characteristic switching time $t_{sw}$ and energy consumption $E_{sw}$ with the device size is shown in Supplementary Fig. 7d. The smaller the device is, the faster switching and the lower energy consumption it achieves.

For the devices with $D = 100$ nm, no perpendicular magnetic anisotropy signals were electrically detected in our experiments, which was also previously reported[18,19], requiring further optimizations in material deposition and device fabrication.

## Supplementary Note 6: Temporal evolution of time-resolved MOKE signal with different compositions

We have measured the devices in the vicinity of the compensation points ($x_{AMC}$ and $x_{MC}$) at room temperature. In the main text, the experimental results are mainly obtained from the devices with the composition of $Co_{76}Gd_{24}$. Under the similar measurement condition with $H_x = 1444$ Oe, $J = 4.2\times10^{11}$ A m$^{-2}$, and $\tau_p = 5$ ns, the temporal evolution of normalized time-resolved MOKE signal are shown in Supplementary Fig. 8 with the composition of $Co_{75}Gd_{25}$ and $Co_{74}Gd_{26}$. The switching time is extracted to be 0.5 and 1.2 ns, respectively.

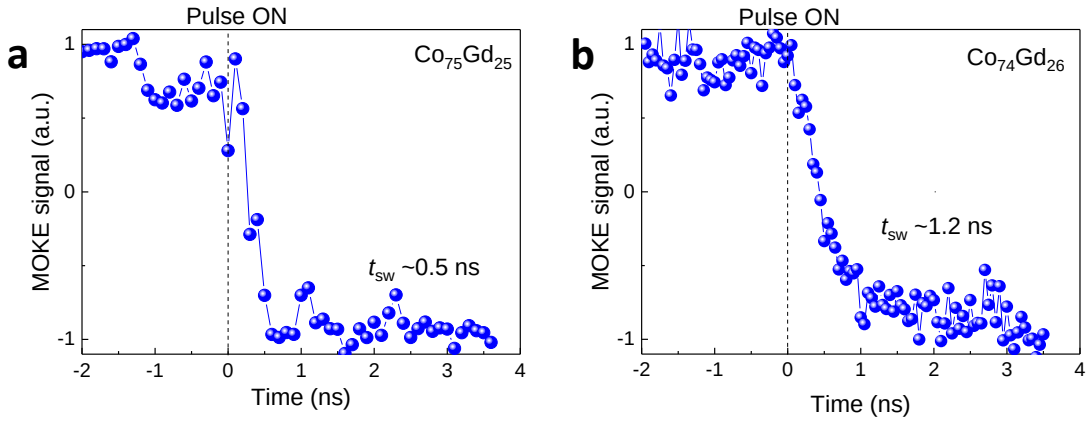


**Supplementary Figure 8 | Time-resolved MOKE signals with different compositions.** The temporal evolution Kerr signal in the devices with the compositions of $Co_{75}Gd_{25}$ (**a**) and $Co_{74}Gd_{26}$ (**b**).

## Supplementary Note 7: Analytical model for domain wall propagation in a ferrimagnetic alloy

The magnetization switching and domain wall motion are strongly related to the angular momentum transfer in the materials. The time-resolved X-ray magnetic circular dichroism (XMCD) measurements demonstrated the ultrafast angular momentum transfer between antiferromagnetically exchange-coupling sublattices[20-22]. In CoTb alloy, a characteristic time of angular momentum transfer is 140 ± 60 fs, corresponding to the timescale of the exchange interaction[20]. The transfer rate of antiferromagnetically coupling link is ~ 5 times larger than that of the ferromagnetically coupling link[23].

First, consider simplified cases with two atomic chains in an ordered system. In the schematic of Supplementary Figs. 9a and b, the system consists of only one type of atom (A or B). In a pure ferromagnetic system, the domain wall propagates at a velocity of $v_{AA}$ (or $v_{BB}$), corresponding to the positive exchange constant $J_{AA}$ (or $J_{BB}$). The systems in Supplementary Figs. 9c and d consist of the same composition of $A_{50}B_{50}$. Supplementary Fig. 9c shows two atomic chains with three kinds of links (A-A, B-B, and A-B links), which ferromagnetic coupling in each chain but antiferromagnetic coupling (A-B links) between the chains. Due to the antiferromagnetic coupling, the magnetization will reverse with a very fast speed between A and B. However, the velocity is limited in the propagation direction by the ferromagnetic links. In Supplementary Fig. 9d, the atoms are alternately arranged with only antiferromagnetic A-B links, which is very similar to the configuration of an antiferromagnet. In this case, a fast switching can happen due to a high domain wall velocity $v_{AB}$. In reality, an alloy is comprised

of randomly distributed atoms, as shown in Supplementary Fig. 9e. Taking advantage of a strong antiferromagnetic couplings between A and B, a relative fast switching can be realized in a ferrimagnet.

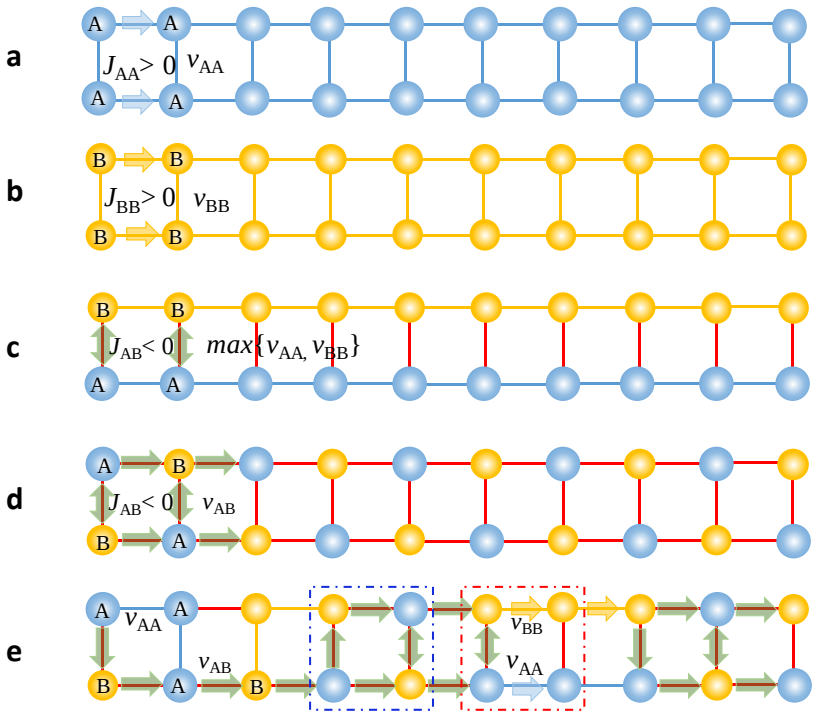


**Supplementary Figure 9 | Model of domain wall propagation. a**, **b**, Schematic illustrations of the domain wall propagation in a pure system with A (or B) atoms. The domain wall propagates to the right side with a velocity of $v_{AA}$ (or $v_{BB}$), corresponding to a positive exchange constant $J_{AA}$ (or $J_{BB}$). **c**, **d**, Schematic illustrations of the domain wall propagation in $A_{50}B_{50}$ system with considering the negative exchange constant $J_{AB}$ due to antiferromagnetic coupling. **e**, Schematic illustration of the domain wall propagation in an alloy system $A_{50}B_{50}$.

Next, we analyse the dynamics of domain wall motion in a ferrimagnetic alloy system shown in Supplementary Fig. 10a using the two-dimensional Ising model. For simplicity, we assume a constant exchange value of $J_{ij}$ for each atomic arrangement ($J_{AA}$, $J_{BB} > 0$ and $J_{AB} < 0$). The simulation was performed over a strip with the dimension of 100 nm×20 nm in the *x*-*y* plane and a distance of 0.4 nm between each atom. The magnetization was fully initialized with $\mathbf{m}_A$ atom along +*z* direction and $\mathbf{m}_B$ along –*z* direction. The domain nucleates at the left side, as shown in Supplementary Fig. 10b. Due to the fast transfer of spin angular momentum between antiferromagnetically coupled A and B atoms, the magnetization switching first propagates along the A-B links, and then expands to the neighbouring atoms thru ferromagnetic links. As the antiferromagnetic coupling links is 10 times faster than that of ferromagnetic links, the total propagation speed is mainly determined by the antiferromagnetic coupling links.

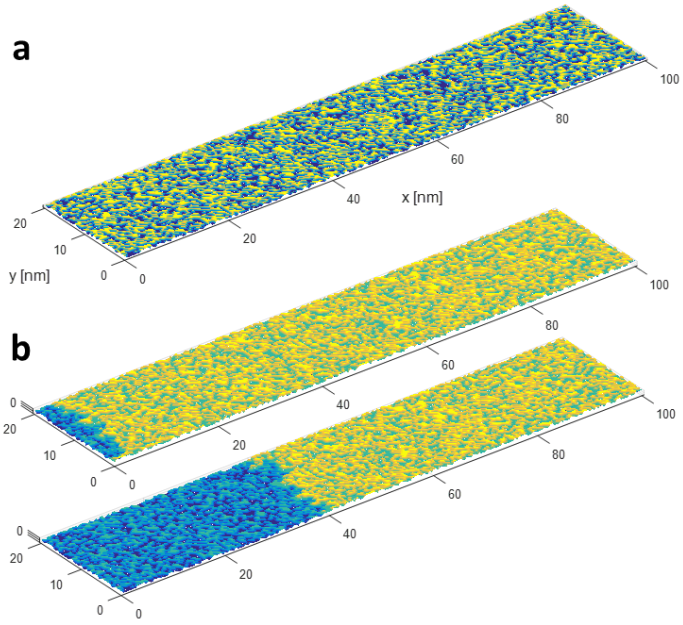


**Supplementary Figure 10 | Simulation results of domain wall propagations in a ferrimagnet. a,** Schematic illustrations of atom distribution in an alloy system $A_{50}B_{50}$. The blue colour represents the A atoms and yellow colour presents the B atoms. **b**, Schematic of the domain propagation. The domain nucleates from the left side and propagates to the right side.

## Supplementary Note 8: Atomistic spin model simulation of domain wall velocity in ferrimagnets

To further understand the fast domain wall motion and the SOT switching in ferrimagnet, we perform the atomistic spin model simulations. The spin–orbit torque driven domain wall motion in ferrimagnets is modelled using a one-dimensional atomistic model[24], which includes simplified antiferromagnetic coupled elements separated at a lattice constant $d$ = 0.4 nm (as shown in Supplementary Fig. 9d). The Hamiltonian is given by

$$H = -A\sum_i \mathbf{S}_i \cdot \mathbf{S}_{i+1} - K_i \sum_i (\mathbf{S}_i \cdot \hat{\boldsymbol{z}})^2 + \kappa_i \sum_i (\mathbf{S}_i \cdot \hat{\boldsymbol{x}})^2 + D_{\mathrm{DMI}} \sum_i \hat{\boldsymbol{y}} \cdot (\mathbf{S}_i \times \mathbf{S}_{i+1}), \qquad \text{(S4)}$$

where $\mathbf{S}_i$ is the lattice-site spin moment normalized to unity, $A$ is the exchange constant, $K_i$ is the easy-axis anisotropy, $\kappa_i$ is the domain wall hard-axis anisotropy, and $D_{\mathrm{DMI}}$ is the Dzyaloshinskii–Moriya interaction (DMI) constant. The spin dynamics of each sublattice is described by the atomistic Landau-Lifshitz-Gilbert (LLG) equation

$$\partial \mathbf{S}_i / \partial t = -\gamma_i \mathbf{S}_i \times \mathbf{B}_{\mathrm{eff},i} + \alpha_i \mathbf{S}_i \times \partial \mathbf{S}_i / \partial t - \gamma_i \hbar J_C \theta_{\mathrm{SH}} / (2eM_{\mathrm{S},i} t_z) \mathbf{S}_i \times (\mathbf{S}_i \times \hat{\boldsymbol{y}}), \qquad \text{(S5)}$$

where $\alpha_i$ is the damping constant, $\hbar$ is reduced Plank's constant, $J_C$ is the charge current density, $\theta_{\mathrm{SH}}$ is the spin-Hall angle, $e$ is the electron charge, $M_{\mathrm{S},i}$ is the saturation magnetization, $t_z$ is the

thickness of the ferrimagnetic layer, $\gamma_i$ is the gyromagnetic ratio and $\mathbf{B}_{\mathrm{eff},i}$ is the effect field. The three terms on the right-hand side are precession, damping, and spin-orbit torque term, respectively. The parameters used in our simulation are summarized as follows[25]: $A = -15$ meV, $K_{\mathrm{TM}} = K_{\mathrm{RE}} = 0.08$ meV, $\kappa_{\mathrm{TM}} = \kappa_{\mathrm{RE}} = 0.08$ μeV, $D_{\mathrm{DMI}} = 0.128$ meV, $\alpha_{\mathrm{TM}} = \alpha_{\mathrm{RE}} = 0.02$, $t_z = 0.4$ nm, $g_{\mathrm{TM}} = 2.2$, $g_{\mathrm{RE}} = 2$, $\theta_{\mathrm{SH}} = 0.2$, $M_{\mathrm{S,TM}} = 7.0\times10^5$ A m$^{-1}$, and $M_{\mathrm{S,RE}} = 6.36\times10^5$ A m$^{-1}$. The atomistic LLG equations are solved using the Runge–Kutta fourth-order method with a time step of 2 fs.

To study the effect of net angular momentum $\delta s = |s_{\mathrm{TM}} - s_{\mathrm{RE}}|$ on the domain wall velocity, we perform numerical simulations with different $\delta s$. With a non-zero $\delta s$, the domain wall velocity increases but saturates, whereas it shows a linear increase for $\delta s = 0$ as shown in Fig. 3d of the main text. These results agree with the theoretical prediction of domain wall motion in ferrimagnets[4], which explains the linear relation at $\delta s = 0$ due to the decoupling of domain wall position and angle. Note that $\delta s$ can be tuned by controlling the composition and temperature in a ferrimagnet.

We also compare the domain wall velocities between a ferromagnet and ferrimagnet by choosing $A_{\mathrm{FM}} = 15$ meV. The calculated results of domain wall velocity in a ferrimagnet are about one or two orders of magnitude larger than that of a ferromagnet. Since most parameters between a ferromagnet and ferrimagnet are kept as the same only except the sign of $A$, we attribute the enhanced domain wall velocity to the antiferromagnetic exchange coupling between atoms.

**Supplementary Note 9: Joule heating effect of current pulses**

When a current pulse is injected, the temperature change of the samples is inevitable due to the Joule heating. As angular momentum $A_{\mathrm{s}}$ strongly depends on the temperature, it is crucial to consider the temperature fluctuation during the current injection. To estimate the temperature change induced by the current pulse, we perform a numerical simulation based on Joule heating and heat transfer model in a solid. An energy balance inside the strip considers the heat generation $Q_g$ and accumulation $Q_a$ as well as heat dissipation $Q_d$. The accumulated heat is defined based on the change of temperature with $\Delta Q_a = C_p m \Delta T$, where $C_p$ is the thermal capacitance, $m$ is the mass of strip. The heat generation $\Delta Q_g$ can be expressed in terms of Joule heating as $\Delta Q_g = I(t)^2 R \Delta t$, where $I(t)$ is the current, $R$ is resistance and $\Delta t$ is a finite time step. By taking all the heat transfer into consideration as shown in Supplementary Fig. 11a, the heat

dissipation is the sum of the thermal transfers to the surroundings (electrodes, substrate, and air) and is given by $\Delta Q_d = \Delta t \sum_i k_i A_i \left(T_i(t) - T_R\right)/L_i$, where $k_i$ is the thermal conductivity, $A_i$ is the cross section area, $L_i$ is the distance, $T_i(t)$ and $T_{\mathrm{RM}}$ are the temperature of the device and the ambient temperature, respectively. The thermal accumulation in $\Delta t$ can be estimated using

$$\Delta Q_a = \Delta Q_g - \Delta Q_d = \left( I(t)^2 R - \sum_i k_i A_i \left(T_i(t) - T_{\mathrm{RM}}\right)/L_i \right) \Delta t. \quad \text{(S6)}$$

Thus, the change of the temperature $\Delta T(t) = \Delta Q_a(t)/C_p m$. The time evolution of temperature $T(t)$ can be estimated by $T(t_n + \Delta t) = \Delta Q_a(t_n)/C_p m + T(t_n)$.

The waveforms of the current pulse are shown in Supplementary Fig. 11b with different time duration $\tau_{\mathrm{p}}$ and amplitude $I_{\mathrm{P}}$. In our experiments, the maximum $I_{\mathrm{p}}$ applied to the CoGd microstrip is ~22 mA, corresponding to a current density of ~$4.2\times10^{11}$ A m$^{-2}$. Other parameters of material properties used in the calculation are summarized as follows: the resistance $R$ = 100 Ω, the density of $\rho = 21.45\times10^3$ kg m$^{-3}$ (ref. [26]), the volume $V$ = 10 μm×3 μm×18 nm = $5.4\times10^{-19}$ m$^{-3}$, thermal capacitance $C_p$ = 135 J kg$^{-1}$ K$^{-1}$, the thermal conductivity of the substrate $k_{\mathrm{s}}$ = 130 W m$^{-1}$ K$^{-1}$ (ref. [27]), the electrodes $k_{\mathrm{m}}$ = 400 W m$^{-1}$ K$^{-1}$ and the air $k_{\mathrm{a}}$ = 0.026 W m$^{-1}$ K$^{-1}$ (ref. [28]). The surroundings are considered as the heat sink at a constant temperature ($T_{\mathrm{RM}}$ = 300 K). The heat flows out of the strip via the substrate with a distance of $d_{\mathrm{s}}$ = 670 μm and a cross section area of $A_s$ = 10 μm×3 μm =30 μm$^2$ and through the electrodes with a distance of $d_m$ = 5 μm with partially covering of $A_m$ = 2 μm×3 μm = 6 μm$^2$. The heat dissipation of the air is relatively small. The equations are solved by substituting the above parameters with a time step of 0.1 ns.

The temperature of the device exhibits a sudden increase as the pulse turns on and a decrease when it turns off (as shown in Supplementary Fig. 11b). Supplementary Fig. 11c shows the maximum of calculated temperature increase as a function of the current pulse amplitude $I_{\mathrm{P}}$ with a duration of 5 ns. Devices with $T_{\mathrm{AMC}} > T_{\mathrm{RM}}$ can experience a transition to $T_{\mathrm{AMC}}$ during the injection of pulse. Figure 4a in the main text shows the domain wall velocity reaches a peak, corresponding to the $T_{\mathrm{AMC}}$.

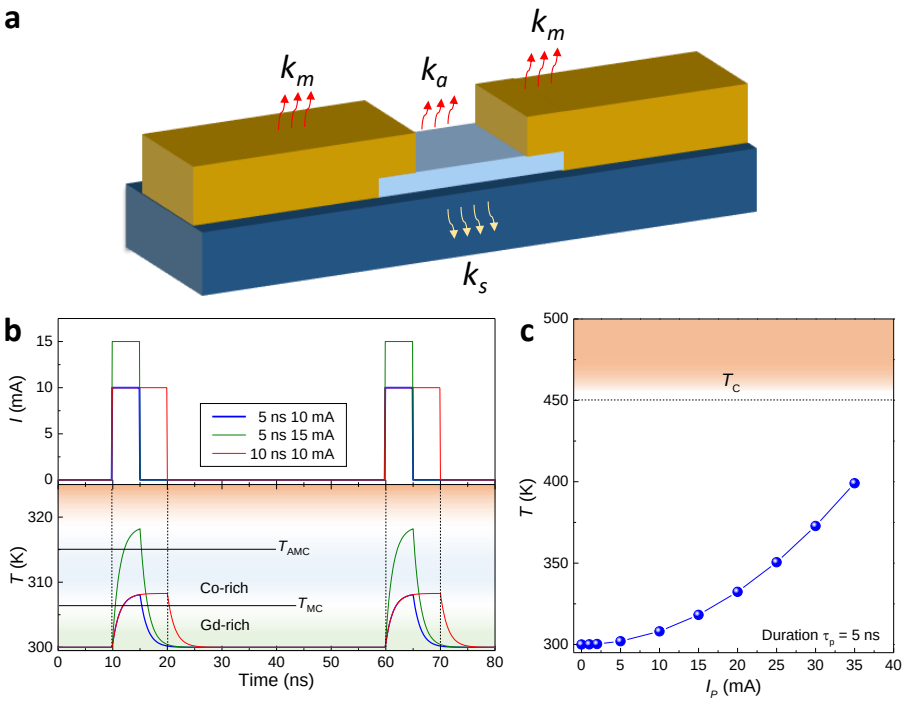


**Supplementary Figure 11 | Simulated Joule heating effect on the magnetic properties of a ferrimagnet. a**, The schematic of heat transfer and dissipation. **b**, The temperature response of the rectangular current pulses with the different duration $\tau_p$ and amplitude $I_P$. **c**, The maximum of calculated temperature as a function of $I_P$ with a duration of $\tau_p$ = 5 ns. The dashed line indicates the Curie temperature $T_C$.

## References


1. Mishra, R. et al. Anomalous current-induced spin torques in ferrimagnets near compensation. *Phys. Rev. Lett.* **118**, 167201 (2017).
2. Siddiqui, S. A., Han, J., Finley, J. T., Ross, C. A. & Liu, L. Current-induced domain wall motion in a compensated ferrimagnet. *Phys. Rev. Lett.* **121**, 057701 (2018).
3. Binder, M. et al. Magnetization dynamics of the ferrimagnet CoGd near the compensation of magnetization and angular momentum. *Phys. Rev. B* **74**, 134404 (2006).
4. Zhu, Z., Fong, X. & Liang, G. Theoretical proposal for determining angular momentum compensation in ferrimagnets. *Phys. Rev. B* **97**, 184410 (2018).
5. Kim, K. J. et al. Fast domain wall motion in the vicinity of the angular momentum compensation temperature of ferrimagnets. *Nat. Mater.* **16**, 1187-1192 (2017).
6. Hirata, Y. et al. Correlation between compensation temperatures of magnetization and angular momentum in GdFeCo ferrimagnets. *Phys. Rev. B* **97**, 220403(R) (2018)
7. Garello, K. et al. Ultrafast magnetization switching by spin-orbit torques. *Appl. Phys. Lett.* **105**, 212402 (2014).
8. Cubukcu, M. et al. Ultra-fast perpendicular spin–orbit torque MRAM. *IEEE Trans. Magn.* **54**, 9300204 (2018).
9. Liu, H. et al. Dynamics of spin torque switching in all-perpendicular spin valve nanopillars. *J. Magn. Magn. Mater.* **358-359**, 233-258 (2014).

10. Lee, J. M. et al. Oscillatory spin-orbit torque switching induced by field-like torques. *Commun. Phys.***1**, 2 (2018).
11. Amiri, P. K. et al. Low write-energy magnetic tunnel junctions for high-speed spin-transfer-rorque MRAM. *IEEE Electron Device Letters* **32**, 57-59 (2011).
12. Baumgartner, M. et al. Spatially and time-resolved magnetization dynamics driven by spin-orbit torques. *Nat. Nanotech.* **12**, 980-986 (2017).
13. Decker, M. M. et al. Time resolved measurements of the switching trajectory of Pt/Co elements induced by spin-orbit torques. *Phys. Rev. Lett.* **118**, 257201 (2017).
14. Yoon, J. et al. Anomalous spin-orbit torque switching due to field-like torque–assisted domain wall reflection. *Sci. Adv.* **3**, e1603099 (2017).
15. Beach, G. S. D., Nistor, C., Knutson, C., Tsoi, M. & Erskine, J. L. Dynamics of field-driven domain-wall propagation in ferromagnetic nanowires. *Nat. Mater.* **4**, 741-744 (2005).
16. Shi, S., Ou, Y., Aradhya, S. V., Ralph, D. C. & Buhrman, R. A. Fast low-current spin-orbit-torque switching of magnetic tunnel junctions through atomic modifications of the free-layer interfaces. *Phys. Rev. Applied* **9**, 011002 (2018).
17. Furuta, M., Okamoto, S., Kikuchi, N., Kitakami, O. & Shimatsu, T. Size dependence of magnetization switching and its dispersion of Co/Pt nanodots under the assistance of radio frequency fields. *J. Appl. Phys.* **115**, 133914 (2014).
18. El-Ghazaly, A. et al. Ultrafast magnetization switching in nanoscale magnetic dots. *Appl. Phys. Lett.* **114**, 232407 (2019).
19. Le Guyader, L. et al. Demonstration of laser induced magnetization reversal in GdFeCo nanostructures. *Appl. Phys. Lett*. **101**, 022410 (2012).
20. Bergeard, N. et al. Ultrafast angular momentum transfer in multisublattice ferrimagnets. *Nat. Commun.* **5**, 3466 (2014).
21. Graves, C. E. et al. Nanoscale spin reversal by non-local angular momentum transfer following ultrafast laser excitation in ferrimagnetic GdFeCo. *Nat. Mater.* **12**, 293-298 (2013).
22. Radu, I. et al. Transient ferromagnetic-like state mediating ultrafast reversal of antiferromagnetically coupled spins. *Nature* **472**, 205-208 (2011).
23. Thielemann-Kühn, N. et al. Ultrafast and energy-efficient quenching of spin order: antiferromagnetism beats ferromagnetism. *Phys. Rev. Lett.* **119**, 197202 (2017).
24. Oh, S.-H. et al. Coherent terahertz spin-wave emission associated with ferrimagnetic domain wall dynamics. *Phys. Rev. B* **96**, 100407(R) (2017).
25. Oh, S.-H. & Lee, K.-J. Ferrimagnetic domain wall motion induced by damping-like spin-orbit torque. *Journal of Magnetics* **23**, 196-200 (2018).
26. Meilikhov;, I. S. G. E. Z. *Handbook of physical quantities*. **116** (1997).
27. Glassbrenner, C. J. & Slack, G. A. Thermal conductivity of silicon and germanium from 3 K to the melting point. *Phys. Rev.* **134**, 1058-1069 (1964).
28. http://periodictable.com/Properties/A/ThermalConductivity.an.html.